UC Irvine

Title

A computational study of aortic reconstruction in single ventricle patients

Permalink

Journal

ISSN

Authors

Taylor-LaPole, Alyssa M
Colebank, Mitchel J
Weigand, Justin D
et al.

Publication Date

DOI

A computational study of aortic reconstruction in single ventricle patients

Alyssa M. Taylor-LaPole[1], **Mitchel J. Colebank**[2], **Justin D. Weigand**[3], **Mette S. Olufsen**[1], **Charles Puelz**[3]

[1]Department of Mathematics, North Carolina State University, Raleigh, NC 27695, USA

[2]Edwards Lifesciences Foundation Cardiovascular Innovation and Research Center, Department of Biomedical Engineering, University of California, Irvine, Irvine, CA 92617, USA

[3]Division of Cardiology, Department of Pediatrics, Baylor College of Medicine and Texas Children's Hospital, Houston, TX 77030, USA

Abstract

Patients with hypoplastic left heart syndrome (HLHS) are born with an underdeveloped left heart. They typically receive a sequence of surgeries that result in a single ventricle physiology called the Fontan circulation. While these patients usually survive into early adulthood, they are at risk for medical complications, partially due to their lower than normal cardiac output, which leads to insufficient cerebral and gut perfusion. While clinical imaging data can provide detailed insight into cardiovascular function within the imaged region, it is difficult to use these data for assessing deficiencies in the rest of the body and for deriving blood pressure dynamics. Data from patients used in this paper include three-dimensional, magnetic resonance angiograms (MRA), time-resolved phase contrast cardiac magnetic resonance images (4D-MRI) and sphygmomanometer blood pressure measurements. The 4D-MRI images provide detailed insight into velocity and flow in vessels within the imaged region, but they cannot predict flow in the rest of the body, nor do they provide values of blood pressure. To remedy these limitations, this study combines the MRA, 4D-MRI, and pressure data with 1D fluid dynamics models to predict hemodynamics in the major systemic arteries, including the cerebral and gut vasculature. A specific focus is placed on studying the impact of aortic reconstruction occurring during the first surgery that results in abnormal vessel morphology. To study these effects, we compare simulations for an HLHS patient with simulations for a matched control patient that has double outlet right ventricle (DORV) physiology with a native aorta. Our results show that the HLHS patient has hypertensive pressures in the brain as well as reduced flow to the gut. Wave intensity analysis suggests that the HLHS patient has irregular circulatory function during light upright exercise conditions and that predicted wall shear stresses are lower than normal, suggesting the HLHS patient may have hypertension.

✉Charles Puelz, charles.puelz@bcm.edu.

Keywords

Hypoplastic left heart syndrome; Fontan circulation; Double outlet right ventricle; Perfusion; Fluid mechanics; Simulation; Systemic circulation

---

1. Introduction

Hypoplastic left heart syndrome (HLHS) is a congenital disease characterized by an underdeveloped left heart. For most of these patients, the left ventricle is non-functional (Tworetzky et al. 2001), i.e. it is unable to generate sufficient cardiac output to perfuse the systemic vasculature with oxygen-rich blood. If left untreated, infants with this defect do not survive. The optimal treatment is a heart transplant, but since few infant hearts are available, patients are usually treated via a sequence of palliative surgeries that result in a single ventricle physiology called the Fontan circulation. Most HLHS patients will eventually require a heart transplant due to failure of the Fontan circuit (Deal and Jacobs 2012). These patients live with a single ventricle pump and therefore do not have the typical capacity for transporting blood throughout the body. Moreover, surgically reconstructed vessels degenerate over time, reducing the ability of the single ventricle to generate sufficient power (Mahle et al. 1998; Voges et al. 2010). The sequence of surgical procedures recommended for this patient population is collectively an attempt to reconstruct and rearrange vessels in the vicinity of the heart so that the single ventricle is functional. These surgeries are the Norwood, Glenn, and Fontan procedures (Voges et al. 2010).

The *Norwood procedure* is performed during the first few weeks of life. This procedure involves the construction of a new aorta, herein referred to as the *reconstructed aorta*. This vessel connects the main pulmonary artery and diminutive native aorta to establish a connection between the single functioning ventricle and systemic circulation. The surgical reconstruction involves the addition of a homograph patch comprised of tissue harvested from the main pulmonary artery (Mahle et al. 1998). Since the reconstructed aorta is attached to the main pulmonary artery, it is necessary to add a shunt to transport blood to the pulmonary circulation for reoxygenation. Two shunts are commonly used: a Blalock-Taussig-Thomas shunt, which connects the subclavian artery or carotid artery to the pulmonary artery, or a Sano shunt, which connects the single ventricle directly to the pulmonary vasculature (Ohye et al. 2010).

The *Glenn procedure* is performed six months after birth. In this surgery, the superior vena cava is connected to the main pulmonary artery to transport venous blood returning from the upper body to the lungs. This new pathway eliminates the need for the shunt placed during the Norwood procedure and it is therefore removed. The resulting circulation mixes oxygenated blood from the pulmonary circulation with deoxygenated blood from the lower body. Mixed blood is subsequently transported to the systemic arteries (Gobergs et al. 2016).

In the *Fontan procedure*, performed at age 18–36 months, the inferior vena cava is connected to the main pulmonary artery, allowing blood from the lower body to also travel to the lungs. The final physiology is characterized by serialized pulmonary and systemic circulations supported by the single functioning ventricle (Fontan and Baudet 1971).

Many HLHS patients live with a single ventricle circulation until early adulthood, but they often experience serious complications, partly as a result of reduced cardiac output (Gewillig and Brown 2016). This leads to insufficient cerebral and gut perfusion comorbid with increased risk of stroke (Saiki et al. 2014) and chronic venous congestion contributing to Fontan-associated liver disease (FALD) (Gordon-Walker et al. 2019; Navaratnam et al. 2016). We hypothesize two important causes of complications: (1) impaired hemodynamic transport driven by the single ventricle and (2) degeneration in the reconstructed vessels over time (Mahle et al. 1998; Gewillig and Brown 2016; Biglino et al. 2012; Mitchell 2018; Bellsham-Revell et al. 2013). We hypothesize that the vessel experiencing the most significant degeneration is the reconstructed aorta. Examination of images (used in this study) clearly shows the aorta in HLHS patients is significantly larger than for the control group comprised of DORV patients. An increase in the aortic cross-sectional area will decrease pressure, requiring the functioning ventricle to pump harder in order to perfuse all essential organs. A cause for aortic degeneration could be the noncompliant patch material harvested from the main pulmonary artery, which does not continue to grow along with the native aortic tissue (Mahle et al. 1998). This might result in vessel remodeling, leading to an increase in vessel stiffness (Ou et al. 2008) and cross-sectional area (Voges et al. 2015). These changes likely lead to increased pulse pressure and the formation of vortices, particularly in the diastolic phase of the cardiac cycle, where flow reversal has been observed (Mitchell et al. 2004; Mitchell 2018).

To examine the impact of aortic remodeling in HLHS patients, we use computational simulations in order to compare hemodynamic predictions in an HLHS patient and DORV patient used as the control. The latter patient has single ventricle physiology but a native aorta, providing an ideal control. Both HLHS and DORV patients in this study have undergone the third and final surgery, the Fontan procedure. Treatments for single ventricle physiology have been investigated heavily in experimental studies. Cardis et al. (2006) examined the impact of aortic reconstruction on elastance properties of the aorta in HLHS, DORV, and other single ventricle patients. Their results demonstrated that reconstructed aortas in HLHS patients had lower distensibility and higher stiffness than the other single ventricle patients. Other experimental studies have examined the effectiveness and timing of the Fontan surgeries (Mainwaring et al. 1994; Tanoue et al. 2001; Yagi et al. 2017). For example, the study by Tanoue et al. (2001) compared results from 18 patients who had the Glenn procedure before the Fontan procedure, with 23 patients who proceeded directly to the total cavopulmonary connection. The authors found that conducting the Glenn procedure first (which is currently recommended) significantly improved patient outcomes. Similar results were found by Mainwaring et al. (1994), who examined concentrations of hormones associated with fluid retention, and Yagi et al. (2017), who measured cerebral oxygenation. Other studies focused on failure of the Fontan circulation. For example, Kotani et al. (2018) studied health records from 500 Fontan patients and found that premature morbidity and death were caused by circulatory failure, multiorgan failure, cerebral/renal issues, and pulmonary failure. They also found that lifespan increased with early intervention and treatment. Saiki et al. (2014) performed a statistical analysis of wave intensity in the carotid artery in 34 patients with a Fontan circulation and 20 controls. Their results showed that

carotid blood flow was much lower in reconstructed Fontan patients than in healthy, double-ventricle controls, suggesting that Fontan patients have lower cerebral perfusion.

Most computational studies examining the Fontan circulation (and its preceding physiologies) use three-dimensional (3D) computational fluid dynamics (CFD) models in order to predict velocity distributions and power losses, mainly through the surgically created connection between the vena cavae and pulmonary arteries (Marsden et al. 2007, 2009; Ahmed et al. 2021). Such simulations are ideal for assessing complex velocity patterns and have been used to explore the effectiveness of various types of Fontan procedures (Bove et al. 2007; Pekkan et al. 2009; Prather et al. 2022; Sun et al. 2014). Bove et al. (2007) and Pekkan et al. (2009) focused on predicting flow distribution and power loss by comparing two second-stage surgeries, the hemi-Fontan and Glenn Procedures. Pekkan et al. (2009) used idealized and patient-specific models and emphasized the importance of examining patient-specific geometries, since results varied significantly between patients, particularly in reconstructed vessels with sharp turns (since these induce high resistance to flow). Recently, Prather et al. (2022) found that in Fontan circuits at risk of failure, the addition of an "injection jet" shunt (IJS) that draws blood from the aortic arch to the lower inferior vena cava can lower venous pressure. Other important computational work includes that of Bazilevs et al. which compares CFD and fluid-structure interaction models of the total cavopulmonary connection in the Fontan circulation (Bazilevs et al. 2009). The authors concluded that the additional detail provided by the fluid-structure interaction model was important for describing hemodynamics in this anatomy.

An alternative computational approach involves one-dimensional (1D) fluid dynamics models which can efficiently predict wave propagation in large networks as well as account for fluid-solid interaction. For example, Puelz et al. (2017) used 1D models to investigate differences between a Fontan circulation with either a fenestration or a hepatic vein exclusion. Their study combined 1D arterial and venous networks with zero-dimensional (0D) heart and organ bed models. They found that both modifications to the Fontan circuit improve flow to the gut. However, their approach did not take into account vortices that may form at bifurcations and in some of the reconstructed vessels. To account for this, an energy loss term can be included in the model with parameters estimated from clinical data (Colebank et al. 2021; Mynard and Valen-Sendstad 2015).

The experimental and computational studies discussed above provide significant insight into complex single ventricle physiology and demonstrate their importance in enhancing our understanding of treatments for HLHS. To our knowledge, there are no computational studies on the effect of aortic reconstruction in HLHS patients that incorporate a comparison to DORV control patients. The goal of this study is to create 1D patient-specific vessel network models that predict blood pressures and flows in regions of interest as well as perfusion to essential organs. Patient-specific networks are constructed from MRA images of two age- and size-matched children; one is an HLHS patient with a reconstructed aorta, and the other is a DORV patient with a native aorta. Both patients have a single ventricle Fontan circulation consisting of the systemic organs and lungs in series Fig. 1. We calibrate models to the 4D-MRI and blood pressure data and then use the calibrated models to predict the

impact of aortic reconstruction on cerebral and gut perfusion, blood pressure, wave intensity, and shear stress.

2. Methods

Vessel dimensions and geometry within the imaged region for the HLHS and DORV patients are extracted from magnetic resonance angiography (MRA) images (Stankovic et al. 2014). To predict the desired quantities, these networks are extended to include all major systemic arteries in the body and brain. To obtain a model that fits to the data, vessels are scaled to patient weight. A one-dimensional (1D) fluid dynamics model is solved in these vessel networks to predict blood flow, pressure, wave intensity, and vessel wall shear stress.

2.1. Data and network geometry

This study uses retrospective hemodynamic measurements from one HLHS and one age- and size-matched DORV control patient. The HLHS patient received a Norwood reconstructed aorta, and both patients had Glenn and Fontan surgeries at the Texas Children's Hospital Heart Center in Houston, Texas. Data collection for this study was approved by the Baylor College of Medicine Institutional Review Board (H-46224: "Four-Dimensional Flow Cardiovascular Magnetic Resonance for the Assessment of Aortic Arch Properties in Single Ventricle Patients"). Patient characteristics, listed in Table 1, include age, height, gender, weight, average resting blood pressure (systolic and diastolic), and cardiac output.

2.1.1. Measurements—Patient data are extracted from high spatial resolution three-dimensional (3D) contrast enhanced magnetic resonance angiography (MRA) images, three-dimensional, time-resolved phase contrast cardiac magnetic resonance (4D-MRI) images, and sphygmomanometer blood pressure measurements. Imaging data include the ascending aorta, aortic arch, brachiocephalic vessels, and descending thoracic aorta. Imaging studies were performed using a 1.5T Siemens Aera magnet (Siemens Healthineers, Erlangen, Germany).

Using localizing sequences from the cardiac MRI, time-resolved, contrast enhanced dynamic MRA was performed with bolus injection of 0.1 mL/kg of intravenous gadolinium contrast. MRA was performed in the sagittal plane over a 30–60 s breath-hold, with 3–7 measurements acquired after contrast administration at a temporal resolution of 3–5 s/measurement based on heart rate. 90–120 slices per measurement were acquired with a slice thickness of 1.2–1.4 mm and reconstructed voxel dimensions of $1.2 \times 1.2 \times 1.2$ mm^3. Images were stored on a password protected server in DICOM format.

Three-dimensional time-resolved phase contrast CMR (4D-MRI) was performed using the gradient echo phase contrast sequence that utilized both ECG and respiratory navigation to allow for free-breathing acquisition. The sequence was prescribed as a sagittal acquisition to cover the entire thoracic aorta and proximal brachiocephalic vessels. The 4D-MRI sequence was acquired with the patient free breathing with a slice thickness of 1–2.5 mm. Velocity encoding was set to 10% above the highest velocity expected in the aorta. The accuracy of the 4D-MRI sequences is in part determined by spatial and temporal resolutions as well as

an adequate signal-to-noise ratio. In an effort to maximize the latter, the 4D-MRI sequence was performed after the acquisition of the MRA since the contrast provided an enhanced signal-to-noise ratio.

4D-MRI post processing was performed using the CVI 42 software (Circle Cardiovascular Imaging, Calgary, CA). The thoracic aorta and proximal brachiocephalic vessels were included in the region of interest. A velocity mask of the aorta was generated and assessed for aliasing in three orthogonal planes. No aliasing was noted on the studies and the aorta was segmented from the surrounding structures. A centerline was established through the aorta and subsequently in the brachiocephalic, subclavian, and carotid arteries. Flow plane slices at specified locations along the aorta were constructed orthogonally to the centerline. For each prescribed flow plane location, a flow waveform was generated by integrating the masked velocity field over the plane. For this study, we extracted eight flow waveforms, one at the inlet of the ascending aorta and seven along the ascending aorta, aortic arch, descending aorta, thoracic aorta, brachiocephalic, left common carotid, and left subclavian arteries (refer to Fig. 2). The eight waveforms along the vessels listed above are shown in Fig. 2a.

Systolic and diastolic cuff pressures and resting heart rates (used to determine the length of one cardiac cycle) were also measured. To ensure the data satisfy conservation of blood flow, the brachiocephalic, subclavian, and left common carotid flow waveforms are scaled. For these smaller imaged vessels, the measured flow waveforms are scaled by multiplying the original waveform by a factor to enforce mass conservation. In addition, we scale the flow measurements in the aorta if the average flow is bigger than the flow in the preceding slice. Average flow values before and after scaling are given in Table 2, and the scaled flow waveforms are shown as dashed lines in Fig. 6. Average flow values are calculated by integrating waveforms over the duration of the cardiac cycle and dividing by that duration. We chose to scale flow waveforms for the smaller imaged vessels because they have smaller cross-sectional area compared to the aorta, and the corresponding smaller velocity mask might give rise to higher uncertainty in the flow predictions. More specifically, the smaller vessels have fewer voxels spanning their cross section. As a result, the cross-sectional areas of these vessels carry higher uncertainty. The volumetric flow rate, obtained by multiplying velocity by cross-sectional area, therefore also has higher uncertainty. Furthermore, vessel waveforms were captured close to bifurcations, where vortices could have been present and which might add more uncertainty to the data.

2.1.2.   Geometric domains—For each patient, vessel dimensions are extracted from the MRA data. Images from the DORV and HLHS patients include the ascending aorta, aortic arch, brachiochephalic trunk, thoracic aorta, subclavian artery, common carotid artery, vertebral artery, and brachial artery. Vessel network extraction requires several steps. The first step is to generate a 3D volume rendering of the large vessels from the MRA image. The second step requires the generation of vessel centerlines, radii, and lengths. The third step involves the organization of these parameters into a labeled graph that consists of edges corresponding to vessels, nodes corresponding to junctions, and radii and lengths for each vessel. Finally, the graph is augmented by attaching the main systemic arterial networks

appearing outside the imaged region. The last step is done by scaling literature values of peripheral vessel networks to patient weight.

3D rendering: Segmentation of the vessel geometries in the imaged region is performed using the open-source software 3DSlicer from Kitware Inc. (Fedorov et al. 2012; Kikinis et al. 2014). A 3D rendered volume is obtained using the built-in thresholding,[1] cutting, and islanding tools. The 3D geometry is saved to STL format and imported into Paraview (Kitware Inc. Utkarsh 2015), where it is converted to a VTK polygonal data file before processing with the Vascular Modeling Toolkit (VMTK, http://www.vmtk.org/) (Antiga et al. 2008).

Centerlines: VMTK generates centerlines from the 3D rendered volume by inscribing spheres within each vessel (Antiga et al. 2008). At each point along the vessel, the radius is determined from the maximally inscribed sphere. VMTK generates centerlines that begin at a manually selected source point (the inlet of the aorta) and terminate at manually selected end points. In each vessel, the software then backtraces centerlines from the end points to the source point. The output from VMTK denotes junctions as the point where two centerlines intersect. For most vessels, this point is not at the center of the vessel junction. To correctly position the junctions, we manually adjust the VMTK-generated junction positions by moving the x, y, z coordinates along the parent vessel (e.g., the aorta) to ensure the daughter vessels (e.g., the carotid artery) intersect the aorta at a right angle. Additional details regarding methodology can be found in Antiga et al. (2008). Centerlines are saved as CSV files and imported into custom Matlab (The MathWorks, Inc., Natick, Massachusetts) software for postprocessing. Centerlines are shown in the 3D rendering of the aorta geometries in Fig. 3, panel (c).

Directed graph: Previously developed algorithms implemented in Matlab are used to construct a labeled graph from the VMTK centerlines (Colebank et al. 2019, 2021). Centerlines are converted to edges, corresponding to vessels, and nodes, corresponding to junctions. Each vessel is added to a connectivity matrix that determines the vessel network topology. Edges include x, y, z coordinates along the centerlines and the corresponding radii determined from the maximally inscribed spheres within the vessel. Vessel length is calculated as a sum of the distances between x, y, z coordinates. Vessel junctions are defined as the intersection of two centerlines, and terminal vessels (corresponding to sites for the structured tree models) are identified as branches with no distal daughter vessels (Fig. 3).

Whole body network: Similar to previous studies by Melis et al. (2019) and Puelz et al. (2017), we use a 57-vessel network that includes all vessels captured in the MRA image. Arteries outside of the imaged region are allometrically scaled from literature data according to patient weight. Vessels in the neck and cerebral circulations are scaled from Melis et al. while vessels in the abdomen and lower body are scaled from Puelz et al. (2017). Figure 3 shows the extracted geometries and extrapolated network used in this study. As suggested by Pennati and Fumero (2000), we scale the vessel length as follows:

---

[1] Image intensities are taken in the range 100–264 Houndsfield Units

$$L_2 = L_1\left(\frac{W_1}{W_2}\right)^\alpha, \tag{1}$$

where $\alpha = 0.35$ and W_1(kg) and L_1(cm) are patient weight and vessel length obtained from literature (Melis et al. 2019; Puelz et al. 2017), respectively, and W_2(kg) is the weight of the DORV or HLHS patient. The quantity L_2(cm) is the unknown vessel length. The inlet radii of vessels immediately outside of the imaged region are matched to the size of the outlet radii of their preceding vessels within the imaged region to ensure continuity of radii along the network. For vessels that are not within the imaged region or immediately outside the imaged region, radii are scaled by the same method as described above.

Large systemic vessels are known to taper along their length (Caro et al. 1978). To account for tapering in our models, we estimate tapering parameters by fitting an exponential function of the following form to data from the descending thoracic aorta:

$$r(x) = n_1\exp(-n_2x) + n_3. \tag{2}$$

In Eq. 2, r denotes the vessel radius (cm), x denotes the axial location along the vessel, n_1 denotes the inlet radius minus the outlet radius, n_2 denotes the average degree of taper, and n_3 denotes the outlet radius. For vessels visible in the angiographic images, values for n_1 and n_3 are determined from the segmentation by fitting the model in Eq. 2 to data. For vessels outside the imaged region, we use literature values (Puelz et al. 2017; Melis et al. 2019) that are adjusted to ensure continuity between the regions, e.g., for the aorta (shown in Fig. 4). We first determine the radius relation for all vessels within the imaged region. From these, we compute an average tapering factor (n_2). This tapering factor is used for all vessels outside the imaged region. For vessels with an inlet within the imaged region, we use data to set the inlet radius and Eq. 1 to scale literature values for the vessel length and outlet radius. For vessels completely outside of the imaged region, Eq. 1 is used to scale the vessel length, inlet radius, and outlet radius based on the patient's weight. Table 3 lists the network and vessel dimensions.

2.2. Fluid dynamics model

Hemodynamics are predicted by solving a one-dimensional (1D) fluid dynamics model that describes blood flow, blood pressure, and vessel cross-sectional area along the vessel's axial dimension in a network of compliant vessels. Solutions to this model are computed explicitly in large vessels within the network, shown in Fig. 3. The microvasculature hemodynamics are predicted using a linearized model that is solved semi-analytically within a structured tree framework. For this study, the microvascular networks provide impedances that are used as boundary conditions for the large vessel network. Below, we describe the models used for the large and small vessel. Parameters for each patient are given in Tables 3 and 4.

2.2.1. Large vessels—The 1D model is derived from the Navier–Stokes equations, assuming axially symmetric Newtonian flow, cylindrical vessels, and that blood is

incompressible, viscous, and homogeneous with constant density $\rho = 1.057\left(g/cm^3\right)$ and viscosity $\mu = 0.032(g/cm/s)$ (Olufsen et al. 2000). The flow $q(x,t)(mL/s)$, the pressure $p(x,t)\left(g/cm/s^2\right)$, and the cross-sectional area $A(x,t)\left(cm^2\right)$ in each vessel satisfies the following 1D mass conservation and momentum balance equations:

$$\frac{\partial A}{\partial t} + \frac{\partial q}{\partial x} = 0, \tag{3}$$

$$\frac{\partial q}{\partial t} + \frac{\partial}{\partial x}\left(\frac{q^2}{A}\right) + \frac{A}{\rho}\frac{\partial p}{\partial x} = -\frac{2\pi v R}{\delta}\frac{q}{A} + gA\cos(\theta) \tag{4}$$

where $0 \leq x \leq L$ is the axial position within the vessel. Here, $v = \frac{\mu}{\rho}\left(cm^2/s\right)$ is the kinematic viscosity, $g\left(cm/s^2\right)$ is the gravitational acceleration, and θ is the angle between the vessel and the gravitational field.

These equations are obtained by using an averaged velocity profile $u_x(r,x,t) = q/A$ along each vessel and by imposing a Stokes boundary layer in Eq. (4) of the form:

$$u_x(r,x,t) = \begin{cases} \bar{u}_x, & r < R - \delta, \\ \bar{u}_x\frac{(R-r)}{\delta}, & R - \delta < r \leq R, \end{cases} \tag{5}$$

where R is the radius of the vessel, $\delta = \sqrt{vT/2\pi}(cm)$ is the boundary layer thickness, $T(s)$ is the cardiac cycle duration, and u_x is the average velocity in the axial direction. The system of equations is closed via a pressure–area relationship for the vessel wall, herein modeled as a linear elastic membrane:

$$p(x,t) - p_0 = \frac{4}{3}\frac{Eh}{r_0}\left(1 - \sqrt{\frac{A_0}{A}}\right). \tag{6}$$

Here, $E\left(g/cm/s^2\right)$ is Young's modulus, $h(cm)$ is vessel wall thickness, $p_0\left(g/cm/s^2\right)$ is the reference pressure, $r_0(cm)$ is the inlet radius, and $A_0\left(cm^2\right)$ is cross-sectional area when the pressure equals its reference value. To account for radius dependent stiffening, we define:

$$\frac{Eh}{r_0} = k_1\exp(-k_2 r_0) + k_3 \tag{7}$$

where $k_1\left(g/cm/s^2\right)$, $k_2(1/cm)$ and $k_3\left(g/cm/s^2\right)$ are constants. Simulated pressures are converted to mmHg using the conversion that 1 mmHg equals 1333.22 g/cm/s^2.

The model described above forms a hyperbolic system of PDEs. Therefore, boundary conditions are required at the inlet and outlet of each vessel. At the inlet of the arterial tree (the ascending aorta), a flow waveform is imposed using the waveform extracted from the 4D-MRI data (refer to Fig. 5). At the junctions, we enforce mass conservation and pressure continuity:

$$q_p = q_{d1} + q_{d2}, \tag{8}$$

$$p_p = p_{d1} = p_{d2}, \tag{9}$$

where subscript p refers to the parent vessel and $di(i = 1, 2)$ refer to the two daughter vessels.

In Eq. (4), the term $gA\cos(\theta)$ accounts for gravitational effects. When modeling patients in a supine position, $\theta = \frac{\pi}{2}$. In this case, all vessels are approximately at the same height as the heart, so gravity does not need to be considered. When modeling patients in an upright position, vessels carrying blood upwards from the heart are assigned $\theta = -\pi$ since blood is working against gravity. Vessels carrying blood downward from the heart are assigned $\theta = 0$, since blood moves with gravity in the positive direction. Vessels moving approximately parallel to the ground are assigned $\theta = \frac{\pi}{2}$.

Similar to our previous studies (Olufsen et al. 2000; Olufsen 2001; Chambers et al. 2020; Colebank et al. 2019, 2021), model equations are non-dimensionalized and solved using the two-step Lax-Wendroff method.

2.2.2. Small vessels—Outflow boundary conditions are attached to each terminal vessel. Similar to our previous studies (Colebank et al. 2021; Olufsen et al. 2000; Olufsen 2001; Chambers et al. 2020), we predict flow to the vascular beds by coupling large vessels to asymmetrical structured trees (Olufsen et al. 2000; Olufsen 2001), as shown in Fig. 7. In the small arteries, viscous forces are dominate inertial forces, allowing us to linearize (3) and (4). The equations are reduced by assuming periodicity of solutions, as described in detail in Olufsen et al. (2000), resulting in:

$$i\omega Q + \frac{A_0(1 - F_J)}{\rho}\frac{\partial P}{\partial x} = 0, \tag{10}$$

$$i\omega CP + \frac{\partial Q}{\partial x} = 0, \tag{11}$$

where $F_J = 2J_1(w_0)/w_0J_0(w_0)$, $J_\ell(w_0)$, $\ell = 0, 1$ are the zeroth and first order Bessel functions, and $w_0^2 = i^3 r_0^2 \omega/v$. Note that $w^2 = r_0^2 \omega/v$ is the Womersley number. A reduced wave equation may be derived by differentiating Eq. (11) and substituting the result into Eq. (10):

$$\frac{\omega^2}{c^2}Q + \frac{\partial^2 Q}{\partial x^2} = 0, \text{ or } \frac{\omega^2}{c^2}P + \frac{\partial^2 P}{\partial x^2} = 0, \tag{12}$$

where $c = \sqrt{A_0(1 - F_J)/\rho C}$ is the wave propagation velocity. Solutions to Eqs. (10) and (11) are:

$$Q = a\cos(\omega x/c) + b\sin(\omega x/c), \tag{13}$$

$$P(x, \omega) = i\sqrt{\frac{\rho}{CA_0(1 - F_J)}}(-a \sin(\omega x/c) + b \cos(\omega x/c)), \qquad (14)$$

where a, b are constants of integration. As was done in the large vessels, boundary conditions need to be defined for the small vessels. Similarly, pressure continuity and mass conservation are preserved. A bifurcation is analogous to a transmission-line network in which the impedances satisfy:

$$\frac{1}{Z_p} = \frac{1}{Z_{d1}} + \frac{1}{Z_{d2}}. \qquad (15)$$

Similar to the original work by Olufsen et al. (2000), we assume the terminal impedance at the end of the structured tree is zero.

2.3. Wave intensity analysis

To quantify the incident (forward-moving) and reflected (backward moving) components of waves, we use wave intensity analysis (WIA) (Colebank et al. 2021; Qureshi et al. 2019a, b). Assuming negligible frictional losses, the incident and reflected waves are approximated by setting $q = Au$, where u(cm/s) is fluid velocity, and defining:

$$\Gamma_\pm(t) = \Gamma_0 + \int_0^T d\Gamma_\pm, \quad \Gamma = p, u \qquad (16)$$

$$dp_\pm = \frac{1}{2}(dp \pm \rho c du), \quad du_\pm = \frac{1}{2}\left(du \pm \frac{dp}{\rho c}\right), \qquad (17)$$

where c(cm/s) is the pulse wave velocity. We defined the time-normalized wave intensity as:

$$WI_\pm = (dp_\pm/dt)(du_\pm/dt). \qquad (18)$$

Incident waves are classified as compressive with $WI_+, dp_+ > 0$ and expansive with $WI_+, dp_+ < 0$. Similarly, reflected waves are classified as compressive with $WI_-, dp_- > 0$ and expansive with $WI_-, dp_- < 0$. The wave reflection coefficient is defined as the ratio of amplitudes of the reflected compression pressure waves to the incident compression pressure waves:

$$I_R = \frac{\Delta p_-}{\Delta p_+}. \qquad (19)$$

Forward compression waves (FCW) begin at the inlet of the vessel and increase the pressure and flow velocity as blood propagates toward the outlet of the vessel. Forward expansion waves (FEW) also begin at the inlet of the vessel but decrease pressure and flow velocity. Backward compression waves (BCW) begin at the outlet of the vessel and propagate

backward down the vessel, increasing pressure but decreasing flow velocity. Backward expansion waves (BEW) decrease pressure while accelerating flow (Colebank et al. 2021).

2.4. Wall shear stress

We compute wall shear stress (WSS) in the large vessels, i.e., the stress the fluid exerts on the vessel wall, denoted $\tau_w (g/cm/s^2)$, by using the Stokes boundary layer given in Eq. (5) (Bartolo et al. 2022). This results in the following equations:

$$\tau_w = -\mu\frac{\partial u}{\partial r}, \tag{20}$$

$$\Rightarrow \tau_w = \begin{cases} 0, & r < R - \delta, \\ \dfrac{\mu\bar{u}}{\delta}, & R - \delta < r \leq R, \end{cases} \tag{21}$$

where μ is blood viscosity and $\delta = \sqrt{vT/2\pi}$ is the boundary layer thickness.

2.5. Model calibration and simulation

Dimensions from Table 3 and inlet flow waveforms (cardiac output and heart rate) mentioned previously Fig. 6 are used to calibrate models for each patient. The same connectivity matrix is defined for both patients, but the vessel length and radii are different. We assume neither patient has microvascular disease at the time of the measurements. Therefore, both patients are assigned the same boundary condition parameters, i.e., the structured tree parameters including the fractal scaling ratios α and β, the minimum radius r_{min}, and the length to radius ratio (lrr). Nominal large vessel stiffness parameters from Olufsen et al. (2000) are manually tuned for each patient to generate flow waveforms and pressure predictions that match both the data from the imaged region and the cuff pressures (refer to Fig. 6). Before tuning parameters, we perform a parametric study to examine the impact of influential model parameters (k_3 and r_{min}) on flow and pressure predictions. For both models, we found that aortic stiffness (k_3) does not significantly affect flow to the brain and gut regions. However, it impacts the pressure. An increase in minimum radius (r_{min}) decreases the resistance, therefore leading to an increase in flow to the brain and gut regions. The combined effect of changing r_{min} and k_3 allows us to adjust flow and pressure to fit the available data. First, r_{min} is adjusted to ensure that the average flow through the vessels matches the data. Then, k_3 is increased to better match the shape, the maximum, and the minimum of the flow waveform to the data. Manual tuning of k_3 is critical to match the cuff pressure data measured in the brachial artery. The HLHS patient's reconstructed aorta is apriori assigned a greater stiffness compared to the DORV patient in order to account for known increases in aortic stiffness for HLHS patients with the Fontan circulation (Ou et al. 2008). The tuned values are listed in Table 4. Small vessel stiffnesses, denoted ks_i in Olufsen et al. (2000), are equal to their large vessel counterparts (i.e., $k_1 = ks_1$, etc.).

Inlet flow waveforms at rest (described in detail in Sect. 2.1.1) for each patient are extracted from the 4D-MRI data. Figure 4 depicts the inlet flow waveforms for each patient at rest

(measured) and at light upright exercise (estimated). To simulate light exercise, we modulate model parameters in a way inspired by Kung et al. (2014). To increase heart rate, we reduce the duration of the cardiac cycle by approximately 40%, resulting in an average heart rate of approximately 150 bpm. This rate agrees with results reported by Kung et al. (2014) as well as average heart rates for females aged 8–18 years (Harkel et al. 2011). In addition, we multiply the inflow waveform by two to increase the cardiac output by approximately 97%. The calibrated model is used to predict $p(x,t)$, $q(x,t)$, and $A(x,t)$ in all 57 vessels in the supine position and during light upright exercise. Using these predictions, we perform WIA to compare forward and backward wave propagation in the two patients. From the flow and area predictions, we calculate WSS in the large vessels. WSS sensed by endothelial cells in the arteries is typically altered in cardiovascular disease, making it an important output quantity.

3. Results

Results are computed for the DORV and HLHS patients using parameters listed in Table 1. Pressure and flow predictions are shown in the aorta and regions of interest, including the brain and gut Figs. 8 and 9. WIA and WSS results are shown along the aorta Figs. 10 and 11.

3.1. Pressure and flow predictions

Simulations under supine rest and light upright exercise conditions are shown in Figs. 8 and 9. Figure 8 shows predictions within the segmented network and Fig. 9 shows predictions in the peripheral network which describes systemic arterial vessels outside of the imaged region.

Model predictions of the systolic/diastolic pressures for the DORV and HLHS patients are 109/68 mmHg and 118/63 mmHg, respectively. Pressures for both patients are in the normotensive range, but the HLHS patient has significantly higher pulse pressure. These pressure predictions agree with measured values listed in Table 1, which are taken in the supine position. The cardiac output, which is 5.08 L/min for the DORV patient and 4.06 L/min for the HLHS patient, is also within the normal range for a healthy bi-ventricular heart. Even though cardiac output is lower for the HLHS patient, as shown in Fig. 4, the pulse flow is similar for the two patients. Since this study imposes flow at the inlet of the ascending aorta, cardiac output is a model input. The same applies to heart rate, which is 91 bpm and 97 bpm for the DORV and HLHS patients, respectively. Predicted blood pressure and flow waveforms in the aorta are shown in Fig. 6, demonstrating that the calibrated models fit measurements for both patients. An exception is in the thoracic aorta for the HLHS patient, where the model predicted pulse flow is less than that of the data, but the average flow from the model and data agree relatively well.

In light upright exercise, differences in blood flow through the aorta between the HLHS and DORV patients become more apparent. Even though the aortic root pulse flow is similar between patients, the descending aortic pulse flow in the HLHS patient is significantly lower compared to the DORV patient Table 5. Figure 9 demonstrates that for both patients, cerebral flow in the MCA and ACA II is similar in supine rest and light upright exercise.

However, there is less flow to the liver and gut in the HLHS patient at rest compared to the DORV patient. The difference in flow to the liver and gut between the DORV and HLHS patients is more dramatic during light upright exercise. Table 5 lists the percentage of blood volume entering these vessels. Values were calculated by dividing the average blood flow through each vessel by the average blood flow through the ascending aorta.

3.2. Wave intensity analysis

Wave intensity profiles for both patients at the midpoint of the aorta are shown in Fig. 10 for both supine rest and light upright exercise conditions. In comparison with the other waves present, each vessel in all cases has a predominant FCW propelling blood down the vessel. In the DORV patient at rest and light upright exercise, the BCWs are small in the aorta. Exercise predictions for the HLHS patient differ from the predictions for the DORV patient in that the BCW are larger, except for the BCW wave in the thoracic aorta. The FCW in the HLHS patient is also decreased compared to the DORV patient. The DORV patient has an increased FEW compared to the HLHS patient at both rest and light upright exercise. The wave reflection coefficients are shown in Table 6. The DORV patient has a consistently smaller wave reflection coefficient compared to the HLHS patient at both rest and light upright exercise.

3.3. Wall shear stress

WSS results in the aorta are shown in Fig. 11. At rest, the DORV patient has a maximum shear stress of $\sim 30 - 35$ g/cm/s^2 and the HLHS patient has a maximum shear stress of $\sim 10 - 15$ g/cm/s^2. During light upright exercise, these maximums are essentially doubled; the DORV patient has a maximum of $\sim 75 - 80$ g/cm/s^2 and the HLHS patient has a maximum of $\sim 30 - 40$ g/cm/s^2.

4.   Discussion

In this study, we described the construction of models to predict blood pressure and flow dynamics in an HLHS patient with a reconstructed aorta and a DORV patient with a native aorta. Cardiac output was lower and pulse pressure was higher in the HLHS patient, compared to the DORV control patient. This prediction was expected in part due to the remodeling and abnormal morphology of the reconstructed aorta, but data for more patients will be necessary in order to draw significant conclusions. Models were calibrated to flow and pressure data from both patients. Calibrated flow predictions agreed with measured waveforms extracted from 4D-MRI data Fig. 6. Pressure predictions were calibrated to sphygmomanometer measurements taken in the supine position.

4.1.   Pressure and flow predictions

Pressure and flow predictions were generated in vessel networks that were extracted from MRA data. Patient-specific inlet flow waveforms derived from 4D-MRI images were used as boundary conditions at the inlet of the ascending aorta Fig. 6. Parameters determining vessel stiffness and peripheral vascular resistance were manually tuned to fit measurements, and model outcomes were calculated using the calibrated models.

Model predictions revealed that blood flow to the liver and gut circulations was significantly lower in the HLHS patient, while flow through the head and neck vessels was similar between patients. The decrease in flow to the liver and gut could be a result of less flow through the descending aorta Fig. 8. Decreased perfusion to the gut for the HLHS patient might explain the more frequent development of FALD in this population (Camposilvan et al. 2008). Decreased flow to the gut for the HLHS patient may also be consistent with the body's adaptive mechanisms that ensure the brain is supplied with an adequate amount of blood (Saiki et al. 2016). Previous studies, including by Navaratnam et al. (2016), have shown that HLHS patients with reconstructed aortas eventually have inadequate perfusion to the brain. In particular, the authors identified a group of adults with a Fontan circulation that experienced reduced oxygen delivery to the systemic circulation under exercise conditions. Furthermore, they found higher cerebral deoxygenation during vigorous exercise. Our model did not show a significant difference in perfusion to the brain between the two patients. This discrepancy might result from our choice to only simulate light upright exercise and to not include the impact of changes in peripheral vascular resistance, compliance, and cardiac contractility imposed by the autonomic control system during vigorous exercise.

Blood pressure for the HLHS patient was higher in the head and neck vessels compared to the gut vessels. These results suggest the presence of hypertension according to a study by Blanco et al. (2017) that predicted cerebral pressures in both normotensive and hypertensive double-ventricle patients. Their normotensive studies predicted a peak pressure of about 100 mmHg in the middle cerebral artery (MCA). Our pressure predictions for the DORV patient in the MCA and ACA II were consistent with these results; our model predicted a peak systolic pressure of approximately 100–115 mmHg. At rest, the systolic pressure predictions for the HLHS patient were approximately 140 mmHg in both the MCA and anterior cerebral artery (ACA) II, with the diastolic pressures around 58 mmHg. These values are slightly hypertensive and could be indicative of peripheral arterial stiffening (Al-Qamari et al. 2020). This result was exacerbated under light upright exercise conditions; the systolic blood pressure in the MCA and ACA II for the HLHS patient was ~190 mmHg. A review by Al-Qamari et al. (2020) found that increased blood pressure not only can lead to remodeling as a compensatory mechanism but can also lead to ischemic damage to the brain and an increased risk of stroke. It is not uncommon for HLHS patients to experience cerebral circulation issues. A study by Kotani et al. (2018) investigated causes of death from a subgroup of Fontan patients over 20 years. Deaths due to cerebral issues, including thromboembolism, were common in patients who survived the Fontan operation. Related 1D modeling studies, including the work by Puelz et al. (2017), demonstrated similar flow and pressure predictions in a Fontan circulation of an HLHS patient. Their results included a maximum flow in the superior mesenteric artery of approximately 15 mL/s. Peak systolic flow in the superior mesenteric artery of our model was around 13 mL/s (data not shown).

4.2. Wave reflections and wall shear stress

WIA is an important tool for assessing circulatory function (Broyd et al. 2015). Results from the HLHS patient at both rest and in light upright exercise showed smaller FCWs and greater BCWs. Exercise conditions made these differences more apparent. Overall, backward traveling waves, which decelerate the flow (see, e.g., Broyd et al. 2015), were of

higher magnitude in the HLHS patient. Pomella et al. (2018) compared WIA results from healthy individuals during rest and exercise. Their results showed an increase in forward traveling waves and a decrease in backward traveling waves during exercise. These findings are consistent with our results for the DORV patient, suggesting that the HLHS patient may have abnormal circulatory function during light upright exercise. Our results for the HLHS patient appear consistent with the results from Schafer et al. (2021). Their study found that HLHS reconstructed patients have decreased FCW and an increased BCW/FCW ratio compared to Fontan patients with other single left ventricle diseases. Values of the wave reflection coefficient (I_R) provide a measure of local wave reflections between the vessel and the downstream vasculature. Our results showed that light upright exercise consistently reduced the reflection coefficient in all vessels for the DORV patient, but are increased in aortic arches I and II and the thoracic aorta for the HLHS patient. Though we do not account for the acute regulatory effects of exercise in our model (e.g., peripheral vasodilation), we still observed a decrease in the wave reflection coefficient that is consistent with prior studies (Pomella et al. 2018).

WSS can provide insight into endothelial mechanotransduction and long-term adaptation due to hyper/hypotension. WSS results for the DORV patient at rest were typical of a healthy individual, with a maximum of 30–35 g/cm s^2 (Callaghan and Grieve 2018). The maximum WSS for the HLHS patient is reduced, which can be indicative of hypertension and vessel wall deformation (Traub and Berk 1998). Yang et al. (2014) investigated the correlation between WSS and hypertension to ultimately determine whether local WSS values can be associated with vascular deformation. They found that hypertensive patients had lower peak WSS values due to an increased arterial diameter as a compensatory mechanism to combat stiffening vessels. The increase in arterial diameter led to stagnate blood flow in patients in their study, as seen in HLHS patients post-Norwood procedure (due to an increased aortic diameter). Low WSS also caused the transcription of genes to downregulate nitric oxide and upregulate endothelin-1, causing vasoconstriction, increased blood pressure, and led to further degradation of the vessel wall by promoting smooth muscle cell growth and causing loss of vessel compliance (Traub and Berk 1998).

Predictions of shear stress have become increasingly important for optimizing patient outcomes. A recent study by Loke et al. (2020) combined model simulations with expert surgeon input to develop a Fontan conduit that minimized hemodynamic forces. The study used computational modeling across several geometries to help minimize power loss, improve hepatic flow, and minimize WSS. However, few have computationally investigated arterial WSS in Fontan patients, as we have done here. Forecasts of WSS from computational models can assist in determining possible interactions between endothelial cell dysfunction and poor outcomes after Fontan surgery.

4.3. Limitations

The computational efficiency of the 1D model used in this paper allows for rapid calibration of the model to clinical data. Another advantage of our modeling approach is the ability to predict flow in the entire peripheral vessel network, including vessels outside of the imaged region. However, this model also has several limitations, particularly for HLHS patients

in which the reconstructed aorta is not cylindrical. In reality, the abnormal morphology of the reconstructed aorta likely contributes to energy loss due to the formation of vortices. A description of energy loss can be included in the 1D model, as was done in several previous studies (Colebank et al. 2021; Mynard and Valen-Sendstad 2015). An energy loss model could then be calibrated by comparing 1D and 3D simulations, e.g., using a 3D fluid-structure interaction (FSI) model for the reconstructed aorta (Bazilevs et al. 2009; Baumler et al. 2020; Griffith and Patankar 2020), or by identifying potential regions with secondary flow directly from 4D-MRI data. Another limitation is the lack of a heart model in our study. We did not include a description of the single ventricle, and instead we used a prescribed inflow waveform derived from 4D-MRI data. Also, we extended the vessel network beyond the imaged region by scaling vessel lengths and radii based on a healthy individual's geometry. However, DORV and HLHS patients could have abnormalities in their systemic circulation. Lastly, the scaling performed for the light upright exercise model corresponded to an average healthy female adolescent. However, heart rate and cardiac output in exercise for HLHS and DORV patients might change to a different degree compared to healthy individuals.

Another limitation is the lack of quantification in the uncertainty and measurement error of our data. Flow velocities derived from the 4D-MRI data were averaged over several cardiac cycles. In addition, flow was not exactly conserved in the original data. This lack of conservation was particularly evident for the HLHS patient. Furthermore, flow within the left common carotid of the DORV patient was lower than the typical physiologic range. These discrepancies might be attributed to separate masks that were used for the ascending/descending aorta and head and neck vessels in order to post-process the 4D-MRI data and/or the uncertainty present in these data. Using the scaled data, we manually tuned our model for each patient. In future studies, we plan to extend our methodology by adding optimization to estimate unknown model parameters. This technique has been used successfully in previous studies (Colebank et al. 2019; Qureshi et al. 2019a). However, in these studies, parameters were estimated by fitting pressure data from one location. Lastly, we had a single pressure measurement from a blood pressure cuff. For better model calibration, it would be useful to have several pressure readings in different vessels or multiple cuff pressure measurements. In this study, we used data from a single HLHS patient and a single DORV patient. This approach allowed for manually model calibration. In the future, we plan to conduct a larger study that includes multiple patients in each group.

5. Conclusion

This study described the construction of models that predict blood pressure and blood flow in a 57-vessel network for the systemic arteries. Models were constructed from MRA data and calibrated to 4D-MRI and sphygmomanometer pressure data for both a DORV patient and an HLHS patient. The calibrated models were used to compute flow and pressure waveforms, perform wave intensity analysis, and predict wall shear stress at rest and during light upright exercise. The two patients in our study had normal cardiac output, blood pressure, and heart rate. The aorta for the HLHS patient was significantly wider than the control patient, and the wall stiffness determined from model calibration was higher. Our results showed that the HLHS patient had decreased flow to the gut and increased cerebral

pressures, and these findings were consistent with the literature. These results were more prominent during light upright exercise. Both patients had similar flow to the brain at rest and during light upright exercise. Results from wave intensity analysis suggested abnormal flow in the HLHS patient with similar magnitude forward and backward traveling waves. Wall shear stress results for the HLHS patient showed low values in the aortic vessels, suggesting the presence of hypertension.

Acknowledgements

References

Ahmed Y, Tossas-Betancourt C, van Bakel PAJ, Primeaux JM, Weadock WJ, Lu JC, Zampi JD, Salavitabar A, Figueroa CA (2021) Interventional planning for endovascular revision of a lateral tunnel Fontan: a patient-specific computational analysis. Front Physiol 12:718254 [PubMed: 34489735]

Al-Qamari A, Adeleke I, Kretzer A, Hogue CW (2020) Pulse Pressure and Perioperative Stroke. Curr Opin Anaesthesiol 32(1):57–63

Antiga L, Piccinelli M, Botti L, EneIordache B, Remuzzi A, Steinman DA (2008) An image-based modeling framework for patient-specific computational hemodynamics. Med Biol Eng Comput 46:1097–1112 [PubMed: 19002516]

Bartolo MA, Qureshi MU, Colebank MJ, Chesler NC, Olufsen MS (2022) Numerical predictions of shear stress and cyclic stretch in pulmonary hypertension due to left heart failure. Biomech Model Mechanobiol 21:363–381 [PubMed: 35037114]

Baumler K, Vedula V, Sailer AM, Seo J, Chiu P, Mistelbauer G, Chan FP, Fischbein MP, Marsden AL, Fleishmann D (2020) Fluid-structure interaction simulations of patient-specific aorta dissection. Biomech Model Mechanobiol 19(5), 1607–1628 [PubMed: 31993829]

Bazilevs Y, Hsu MC, Bension DJ, Sankaran S, Marsden AL (2009) Computational fluid-structure interaction: methods and application to a total cavopulmonary connection. Comput Mech 45:77–89

Bellsham-Revell HR, Tibby SM, Bell AJ, Witter T, Simpson J, Beerbaum P, Anderson D, Austin CB, Greil GF, Razavi R. (2013) Serial magnetic resonance imaging in hypoplastic left heart syndrome gives valuable insight into ventricular and vascular adaptation. J Am Coll Cardiol 61:561–570 [PubMed: 23273398]

Biglino G, Schievano S, Steeden JA, Ntsinjana H, Baker C, Khambadkone S, de Leval MR, Hsia T-Y, Taylor AM, Giardina A (2012) Reduced ascending aorta distensibility relates to adverse ventricular mechanics in patients with hypoplastic left heart syndrome: noninvasive study using wave intensity analysis. J Thorac Cardiovascu Surg 144:1307–1314

Blanco PJ, Muller LO, Spence JD (2017) Blood pressure gradients in cerebral arteries: a clue to pathogenesis of cerebral small vessel disease. Stroke Vasc Neurol 2(3), 108–117 [PubMed: 28989801]

Bove EL, de Leval MR, Migliavacca F, Balossino R, Dubini G. (2007) Toward optimal hemodynamics: computer modeling of the Fontan circuit. Pediatr Cardiol 28:477–481 [PubMed: 17763891]

Broyd CJ, Davies JE, Escaned JE, Hughes A, Parker K (2015) Wave intensity analysis and its application to the coronary circulation. Glob Cardio Sci 215(5):64

Callaghan FM, Grieve SM (2018) Normal patterns of thoracic aortic wall shear stress measured using four-dimensional flow MRI in a large population. Am J Physiol - Heart Circ Physiol 315(5):1174–1181

Camposilvan S, Milanesi O, Stellin G, Pettenazzo A, Zancan L, D'Antiga L (2008) Liver and cardiac function in the long term after Fontan operation. Ann Thorac Surg 86(1):177–182 [PubMed: 18573420]

Cardis BM, Fyfe DA, Mahle WT (2006) Elastic Properties of the Reconstructed Aorta in Hypoplastic Left Heart Syndrome. Ann Thorac Surg 81(3):988–991 [PubMed: 16488707]

Caro CG, Pedley TJ, Schroter RC, Seed WA (1978) The Mechanics of the Circulation. Oxford University Press

Chambers MJ, Colebank MJ, Qureshi MU, Clipp R, Olufsen MS (2020) Structural and hemodynamic properties of murin pulmonary arterial networks under hypoxia-induced pulmonary hypertension. Proc Inst Mech Eng H 234(11):1312–1329 [PubMed: 32720558]

Colebank MJ, Paun M, Quershi MU, Chesler N, Husmeier D, Olufsen MS, Fix LE (2019) Influence of image segmentation on one-dimensional fluid dynamics predictions in the mouse pulmonary arteries. J. R. Soc. Interface 16:20190284 [PubMed: 31575347]

Colebank MJ, Qureshi MU, Olufsen MS (2019) Sensitivity analysis and uncertainty quantification of 1-D models of pulmonary hemodynamics in mice under control and hypertensive conditions. Int J Numer Method Biomed Eng 37:e3424

Colebank MJ, Qureshi MU, Rajagopal M, Krasuski RA, Olufsen MS (2021) A multiscale model of vascular function in chronic thromboembolic pulmonary hypertension. Am J Physiol-Heart Circ Physiol 321:H318–H338 [PubMed: 34142886]

Deal BJ, Jacobs ML (2012) Management of the failing Fontan circulation. Heart 98: 1098–1104 [PubMed: 22739639]

Fedorov A, Beichel R, Kalpathy-Cramer J, Finet J, Fillion-Robin J, Pujol S, Bauer C, Jennings D, Fennessy F, Sonka M, Buatti J, Aylward S, Miller JV, Peiper S, Kikinis R (2012) 3D Slicer as an image computing platform for the Quantitative Imaging Network. Magn Reson Imaging 20(9):1323–1341

Fontan F, Baudet E (1971) Surgical repair of tricuspid artesia. Thorax26:240–248 [PubMed: 5089489]

Gewillig M, Brown SC (2016) The Fontan circulation after 45 years: update in physiology. Heart 102:1081–1086 [PubMed: 27220691]

Gobergs R, Salputra E, Lubaua I (2016) Hypoplastic left heart syndrome: a review. Acta Med Litu 23(2):86–89 [PubMed: 28356795]

Gordon-Walker TT, Bove K, Veldtman G (2019) Fontan-associate liver disease: A review. J Cardiol 74(3):223–232 [PubMed: 30928109]

Griffith BE, Patankar NA (2020) Immersed Methods for Fluid-Structure Interaction. Annu Rev Fluid Mech 52:421–428 [PubMed: 33012877]

Harkel ADJT, Takken T, van Osch-Gevers M, Helbing WA (2011) Normal values for cardiopulmonary exercise testing in children Eur J. Prev Cardiol 18(1):48–54

Kikinis R, Pieper SD, Vosburgh K (2014) 3D slicer: a platform for a subject-specific image analysis, visualization, and clinical support. In: Jolesz FA (ed) Intraoperative imaging image-guided therapy. Springer, New York, pp 277–289

Kotani Y, Chetan D, Zhu J, Saedi A, Zhao L, Mertens L, Redington AN, Coles J, Caldarone CA, Arsdell GSV, Honjo O. (2018) Fontan failure and death in contemporary Fontan circulation: analysis from the last two decades. Ann Thorac Surg 105:1240–1247 [PubMed: 29397930]

Kung E, Pennati G, Migliavacca F, Hsia T, Figliola R, Marsden A, Giardini A (2014) A simulation protocol for exercise physiology in Fontan patients using a closed loop lumped parameter model. J Biomech Eng 136(8):081007

Loke YH, Kim B, Mass P, Opfermann JD, Hibino N, Krieger A et al. (2020) Role of surgeon intuition and computer-aided design in Fontan optimization: A computational fluid dynamics simulation study. J Thorac Cardiovasc Surg 160(1):203–212.e2 [PubMed: 32057454]

Mahle WT, Rychik J, Weinberg PM, Cohen MS (1998) Growth characteristics of the aortic arch after the Norwood operation. J Am Coll Cardiol 32(7):1951–1954 [PubMed: 9857877]

Mainwaring RD, Lamberti JJ, Moore JW, Billman GF, Nelson JC (1994) Comparison of the Hormonal Response After Bidirectional Glenn and Fontan Procedures. Ann Thorac Surg 57:59–64 [PubMed: 8279919]

Marsden AL, Bernstein AJ, Reddy VM, Shadden SC, Spilker RL, Chan FP, Taylor CA, Feinstein JA (2009) Evaluation of a novel Y-shaped extracardiac Fontan baffle using computational fluid dynamics. J Thorac Cardiovasc Surg 137:394–403 [PubMed: 19185159]

Marsden AL, Vignon-Clementel IE, Chan FP, Feinstein JA, Taylor CA (2007) Effects of exercise and respiration on hemodynamic efficiency in CFD simulations of the total cavopulmonary connection. Ann Biomed Eng 35:250–263 [PubMed: 17171509]

Melis A, Moura F, Larrabide I, Janot K, Clayton RH, Narata AP, Marzo A (2019) Improved biomechanical metrics of cerebral vasospasm identified via sensitivity analysis of a 1D cerebral circulation model. J Biomech 90:24–32 [PubMed: 31064657]

Mitchell GF (2018) Aortic stiffness, pressure and flow pulsatility, and target organ damage. J Appl Physiol 125(6), 1871–1880 [PubMed: 30359540]

Mitchell GF, Parise H, Vita JA, Larson MG, Warner E, Keaney JF Jr, Keyes MJ, Levy D, Vasan RS, Benjamin EJ (2004) Local Shear Stress and Brachial Artery Flow-Mediated Dilation. Hypertension 44:134–139 [PubMed: 15249547]

Mynard JP, Valen-Sendstad K (2015) A unified method for estimating energy losses at vascular junctions. Int J Numer Meth Biomed Eng 31:e02717

Navaratnam D, Fitzsimmons S, Grocott M, Rossiter HB, Emmanuel Y, Diller G, Gordon-Walker T, Jack S, Sheron N, Pappachan J, Pratap JN, Vettukattil JJ, Veldtman G (2016) Exercise-Induced Systemic Venous Hypertension in the Fontan Circulation. Am J Cardio 117:1667–1671

Ohye RG, Sleeper LA, Mahony L, Newburger JW (2010) Comparison of shunt types in the norwood procedure for single-ventricle lesions. N Engl J Med 362:1980–1992 [PubMed: 20505177]

Olufsen MS (2001) A one-dimensional fluid dynamic model of the systemic arteries. In: Fauci LJ, Gueron S (eds) Computational Modeling in Biological Fluid Dynamics The IMA Volumes in Mathematics and its Applications, vol 124. Springer, New York

Olufsen MS, Peskin CS, Kim WY, Pedersen EM, Nadim A, Larsen J (2000) Numerical Simulation and experimental Validation of Blood Flow in Arteries with Structured-Tree Outflow Conditions. Ann Biomed Eng 28:1281–1299 [PubMed: 11212947]

Ou P, Celermajer DS, Jolivet O, Buyens F, Herment A, Sidi D, Bonnet D, Mousseaux E (2008) Increased central aortic stiffness and left ventricular mass in normotensive young subjects after successful coarctation repair. Am Heart J 155(1), 187–193 [PubMed: 18082512]

Pekkan K, Dasi LP, De Zelicourt D, Sundareswaran KS, Fogel MA, Kanter KR, Yoganathan AP (2009) Hemodynamic performance of stage-2 univentricular reconstruction: Glenn vs. Hemi-Fontan templates. Ann Biomed Eng 37(1):50–63 [PubMed: 18987974]

Pennati G, Fumero R (2000) Scaling approach to study the changes through the gestation of human fetal Cardian and circulatory behaviors. Ann Biomed Eng 28:442–452 [PubMed: 10870901]

Pomella N, Wilhelm EN, Kolyva C, Gonzalex-Alonso J, Rakobowchuk M, Khir AW (2018) Noninvasive assessment of the common carotid artery hemodynamics with increasing exercise work rate using wave intensity analysis. Am J Physiol Heart Circ Physiol 315:233–241

Prather R, Das A, Farias M, Divo E, Kassab A, DeCampil W (2022) Parametric investigation of an injection-jet self-powered Fontan circulation. Sci Rep 12:2161 [PubMed: 35140260]

Puelz C, Acosta S, Rivieere B, Penny DJ, Brady KM, Rusin CG (2017) A computational study of the Fontan circulation with fenestration or hepatic vein exculsion. Comput Biol Med 89:405–418 [PubMed: 28881280]

Qureshi MU, Colebank MJ, Paun LM, Fix LE, Chelser N, Haider MA, Hill NA, Husmeier D, Olufsen MS (2019) Hemodynamic assessment of pulmonary hypertension in mice: a model-based analysis of the disease mechanism. Biomech Model Mechanobiol 18(1), 219–243 [PubMed: 30284059]

Qureshi MU, Colebank MJ, Paun LM, Chesler N, Haider MA, Hill NA, Husmeier D, Olufsen MS (2019) A computational study of pulmonary hemodynamics in healthy and hypoxic mice. arXiv: 1712.01699

Saiki H, Kurishima C, Masutani S, Senzaki H (2014) Cerebral circulation in patients with Fontan circulation: assessment by carotid arterial wave intensity and stiffness. Ann Thoracic Surg 97(4):1394–1399

Saiki H, Sugimoto M, Kuwata S, Kurishima C, Iwamoto Y, Ishido H, Masutani S, Senzaki H (2016) Novel mechanisms for cerebral blood flow regulation in patients with congenital heart disease. Am Heart J 172:152–159 [PubMed: 26856227]

Schafer M, Frank BS, Jacobssen R, Rausch CM, Mitchell MB, Jaggers J, Stone ML, Morgan GJ, Browne LP, Barker AJ, Hunter KS, Ivy DD, Younoszai A, Di Maria MV (2021) Patients with Fontan circulation have abnormal aortic wave propagation patterns: A wave intensity analysis study. Int J Cardio 322:158–167

Stankovic Z, Allen BD, Garcia J, Jarvis KB, Markl M (2014) 4D flow imaging with MRI. Cardiovascular Diagn Ther 4(2):173–192

Sun Q, Liu J, Qian Y, Zhang H, Wang Q, Sun Y, Hong H, Lie J (2014) Computational haemondynamic analysis of patient-specific virtual operations for total cavopulmonary connection with dual superior venae cavae. European J Cardio-Thorac Surg 45(3):564–469

Tanoue Y, Sese A, Ueno Y, Joh K, Hihii T. (2001) Bidirectional Glenn procedure improves the mechanical efficiency of a total cavopulmonary connection in high-risk Fontan candidates, Circulation. 103(21), 2176–2180 [PubMed: 11331259]

Traub O, Berk BC (1998) Laminar Shear Stress: Mechanisms by Which Endothelial Cells Transduce an Atheroprotective Force. ATVB 18:677–685

Tworetzky W, McElhinney DB, Reddy MV, Brook MM, Hanley FL, Silverman NH (2001) Improved Surgical Outcome After Fetal Diagnosis of Hypoplastic Left Heart Syndrome. Circulation 103:1269–1273 [PubMed: 11238272]

Utkarsh A (2015) The Paraview guide: a parallel visualization application. Kitware Inc, Clifton Park

Voges I, Jerosch-Herold M, Hedderich J, Westphal C, Hart C, Helle M, Scheewe J, Pardun E, Kramer H, Rickers C (2010) Maladaptive Aortic Properties in Children After Palliation of Hypoplastic Left Heart Syndrome Assessed by Cardiovascular Magnetic Resonance Imaging. Circulation 122:1068–1076 [PubMed: 20805434]

Voges I, Jerosch-Herold M, Wegner P, Hart C, Gabbert D, Bulushi AA, Fischer G, Andrade AC, Pham HM, Kristo I, Kramer HH, Rickers C (2015) Frequent dilation of the descending aorta in children with hypoplastic left heart syndrome relates to decreased aortic arch elasticity. J Am Heart Assoc 4(10):e002107 [PubMed: 26438562]

Yagi Y, Yamamota M, Saito H, More T, Morimoto Y, Oyasu T, Tachibana T, Ito YM (2017) Changes of cerebral oxygenation in sequential Glenn and Fontan procedures in the same children. Pediatric Cardiol 38:1215–1219

Yang JW, Cho KI, Kim JH, Kim SY, Kim CS, You GI, Lee JY, Choi SY, Lee SW, Kim HS, Heo JH, Cha TJ, Lee JW (2014) Wall shear stress in hypertensive patients is associated with carotid vascular deformation assessed by speckle tracking strain imaging. Clin Hypertens 20(10), 1–6
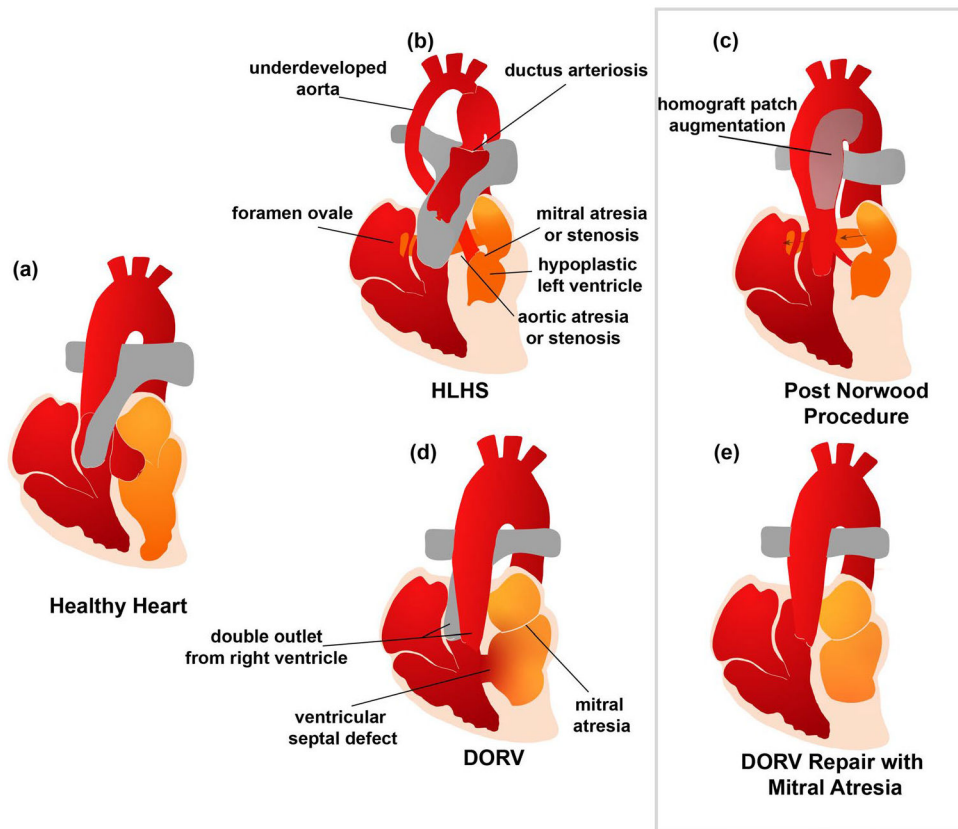
Fig. 1.
Schematic comparison of the physiology of a healthy heart, an HLHS heart, a DORV heart, and HLHS and DORV hearts after the Norwood procedure. **a** A healthy heart with the aorta attached to the left ventricle and the pulmonary artery to the right ventricle. **b** HLHS heart at birth has an underdeveloped aorta, an underdeveloped left ventricle, an extra vessel connecting the pulmonary artery, and the aorta (the ductus arteriosis), and a hole connecting the left and right atria (the foramen ovale). **c** During the Norwood procedure, a homograft patch augmentation is used to construct a new aorta (termed the reconstructed aorta), which is attached to the functioning single ventricle. The native underdeveloped aorta emanating from the left ventricle is kept in order to perfuse the coronary arteries. **d** The DORV heart at birth has both the pulmonary artery and aorta attached to the right ventricle. **e** DORV physiology after the first procedure. No aortic intervention is necessary for DORV single ventricle variants since the native aorta suffices to provide systemic output. The gray box highlights the major difference (the size of the aorta) between the two patients studied
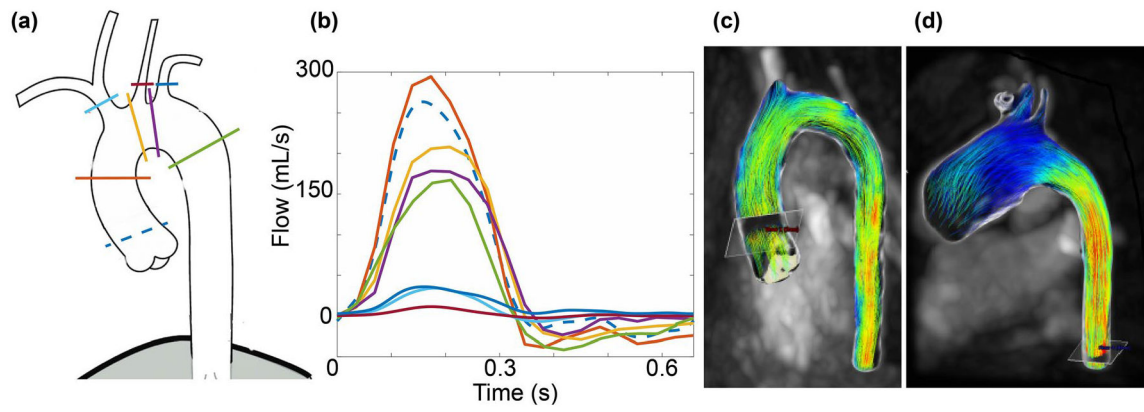
Fig. 2.
a Sketch of the aorta and the planes on which the flow data was measured. Note the inflow waveform at the root (marked by a dashed line) is used as an inlet boundary condition, while the remaining seven flow waveforms are used for model calibration. **b** Flow waveforms for the DORV patient. The dashed waveform denotes the flow at the aortic root. **c** Flow velocity streamlines in the DORV patient. **d** Flow velocity streamlines in the HLHS patient
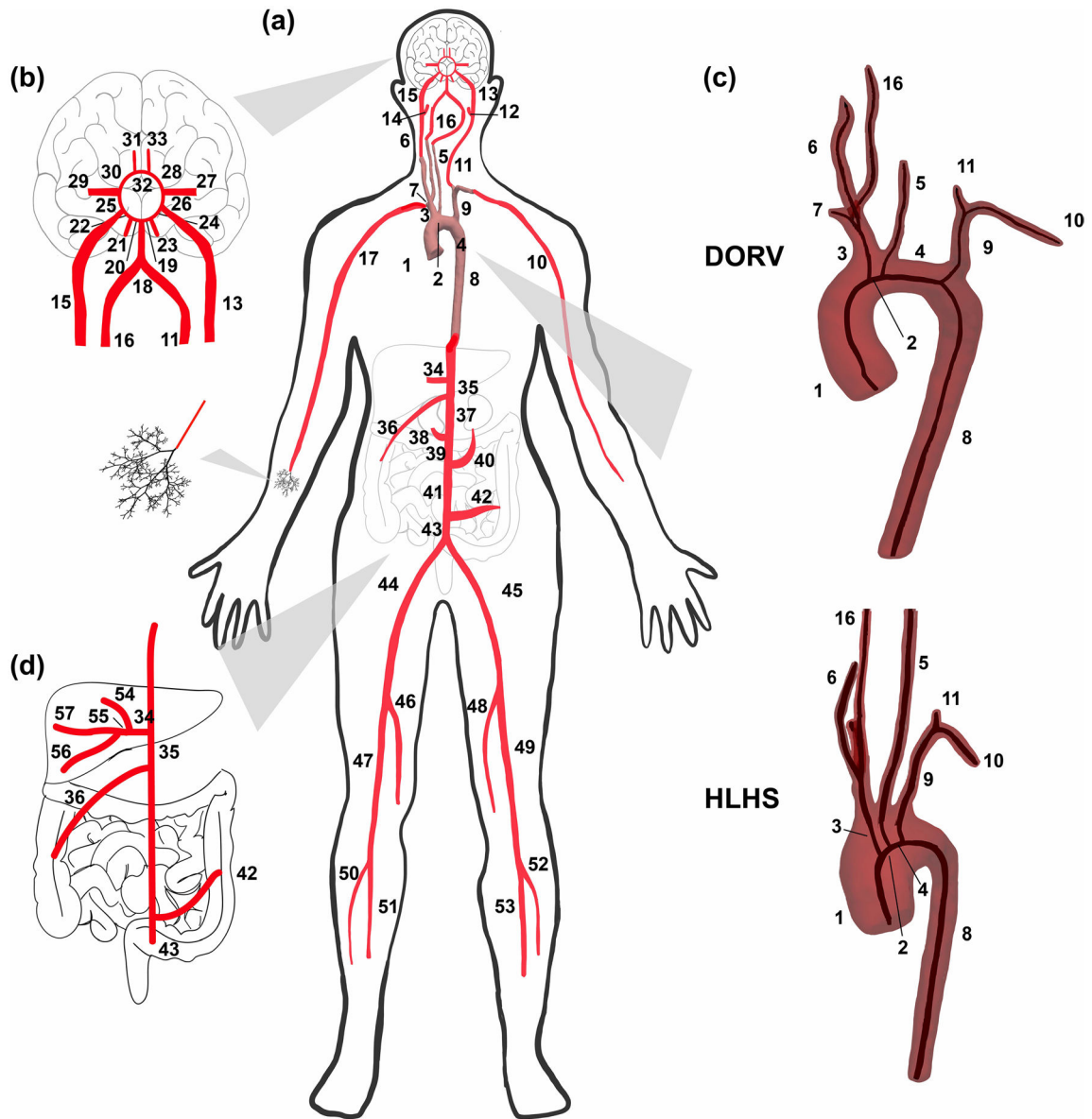
Fig. 3.
The network used for our patient-specific model. The 3D rendered images of the aorta are segmented from the MRA data. **a** The entire network, including vessels outside the imaged region. The latter are calibrated using allometric scaling of literature values and patient weight. Attached to each terminal vessel is a structured tree model, shown on the right arm. **b** A detailed view of the cerebral circulation. **c** 3D renderings of the DORV and HLHS reconstructed patient aortas and nearby vasculature. Vessel centerlines are represented by the darker line through each segmentation. The ascending aorta from the HLHS patient has a much greater radius than that of the DORV. This difference is also apparent in Table 3 with reference to the vessel radii. **d** A detailed view of the gut circulation included in this model
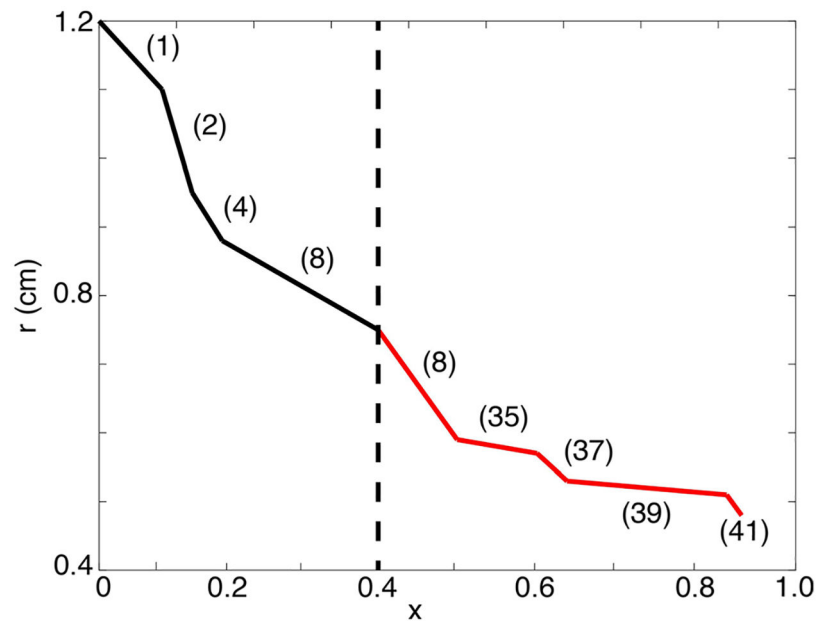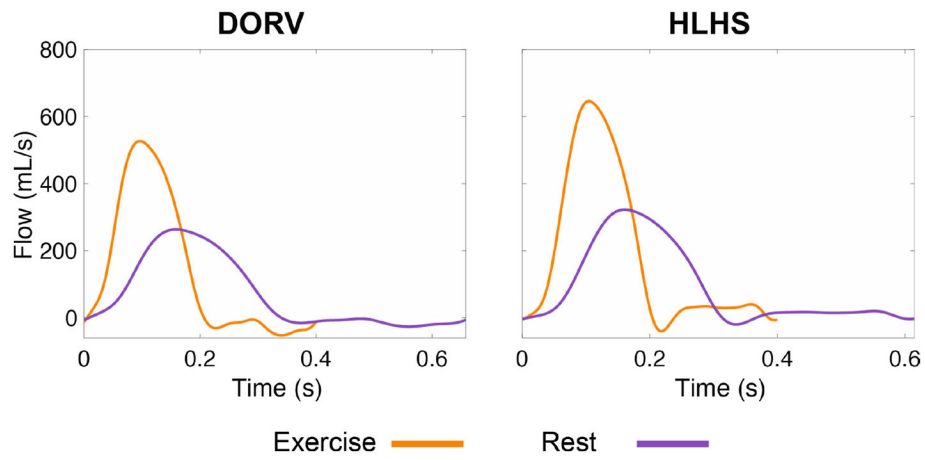
Fig. 4.
Radii along all vessels in the aorta. Vessels outside the imaged region are marked with red.
The vessel number is listed beside the corresponding vessels' radii

Fig. 5.
Inflow profiles for the DORV and HLHS patients at rest and light upright exercise conditions. Inflows at rest are extracted from 4D-MRI data. To simulate light upright exercise, inflow waveforms are multiplied by two and the duration of the cardiac cycle is shortened. At rest, DORV flow reaches about 300 mL/s at the inlet and under exercise conditions the inflow is doubled to reach about 600 mL/s at the inlet. At rest, HLHS flow reaches about 390 mL/s and under exercise conditions is doubled to about 680 mL/s
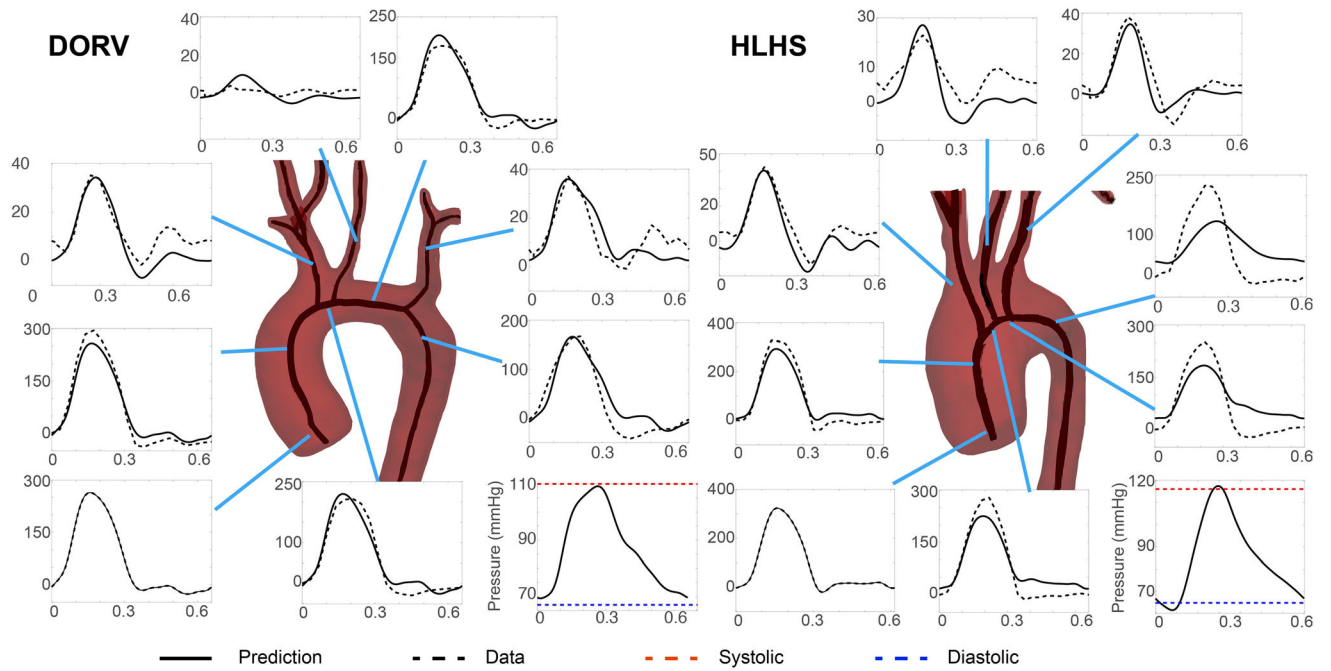
Fig. 6.

Flow and pressure waveforms. Flows derived from the 4D-MRI data are shown as dashed lines, and flows predicted by the models are shown as solid lines. Measured flow data are scaled to ensure conservation of flow required for the 1D model predictions. For all plots of flow, the time units (*x*-axis) are in seconds and the flow units (*y*-axis) are in mL/s. Cuff pressure measurements are obtained for each patient and shown in the bottom right panels in red (systolic) and blue (diastolic). These pressure measurements are taken in the upper left arm. The model pressure predictions, from the upper brachial artery, are shown in the black solid line
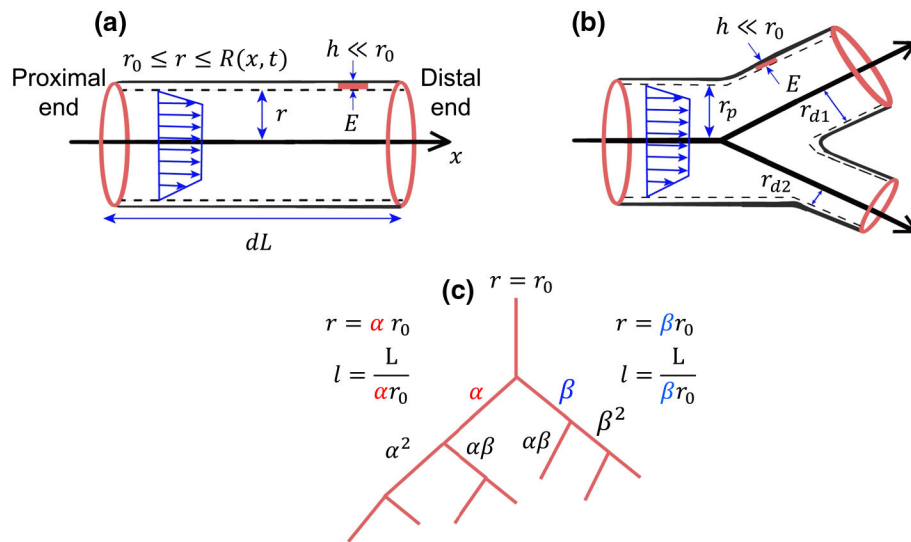
Fig. 7.
Illustration of the vessels modeled in this study. **a** The fluid dynamics of the large vessels and **b** a junction within the large vessels. The region between the dashed and outermost solid lines in **a** and **b** denotes the vessel wall thickness, h(cm), of the vessel. The assumed velocity profile used to reduce the equations to 1D is shown with blue arrows at the proximal ends of the vessel. **c** The structured tree used the terminal vessels
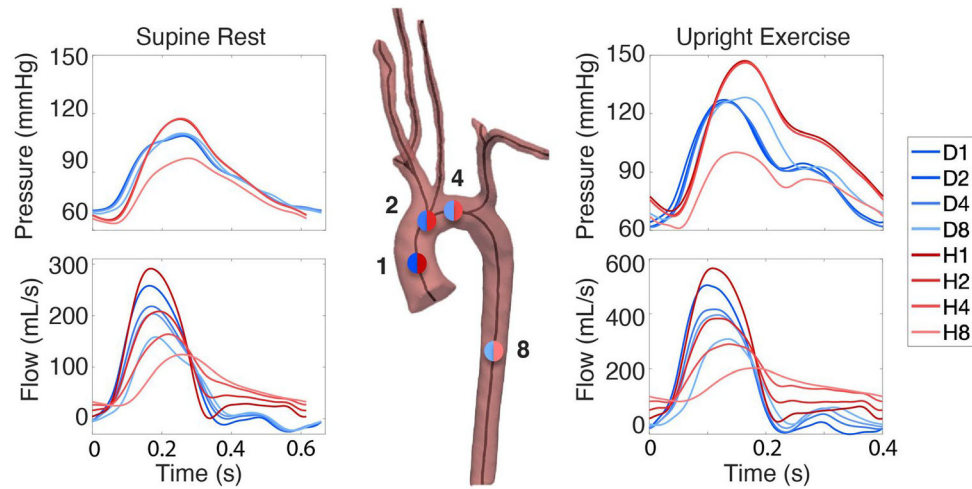
Fig. 8.
Localized pressure and flow predictions in the imaged region. Pressure for the DORV patient ranges from 65 to 105 mmHg at supine rest. A greater range is seen in the HLHS patient, from 63–118 mmHg at supine rest. Cardiac output is similar in the aorta at supine rest and light upright exercise. Predictions deviate significantly in the distal part of the descending aorta. D1, D2, D4, and D8 denote predictions for the DORV patient, and H1, H2, H4, and H8 for the HLHS patient. Note that the flow predictions vary from − 20 to 300 mL/s at supine rest and from − 40 to 600 mL/s during light exercise higher pulse pressure.
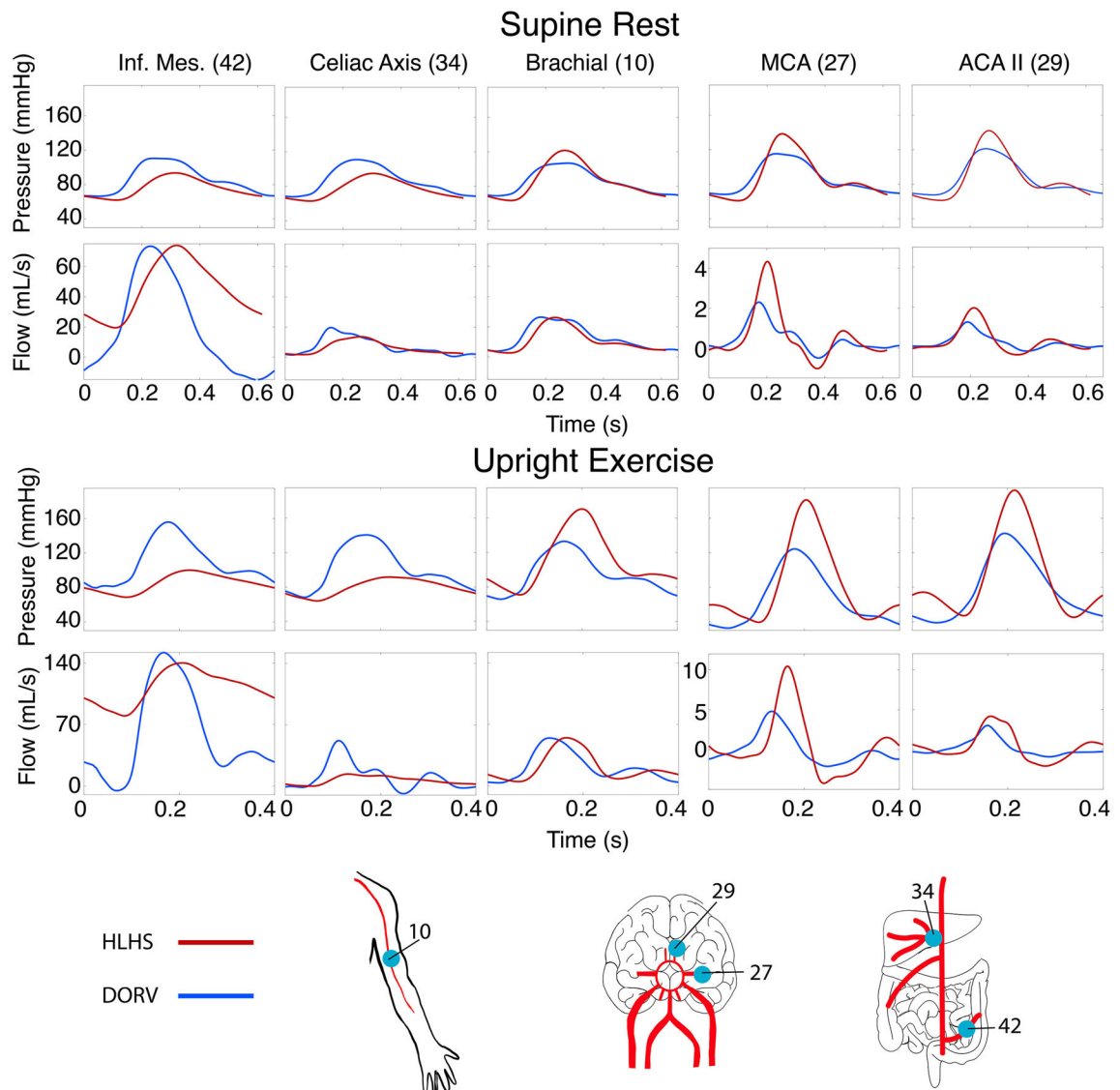
Supine Rest

Fig. 9.
Pressure and flow predictions in supine rest and light upright exercise positions for different vessels. Cerebral pressures are greater in the HLHS patient, but the flow is similar at rest and exercise. In the gut, the pressure and flow are reduced in the HLHS patient compared to the DORV patient. Note the scale changes for the flow plots. Under supine rest, the scale ranges from − 10 to 70 mL/s, and during light upright exercise, it ranges from 0 to 180 mL/s
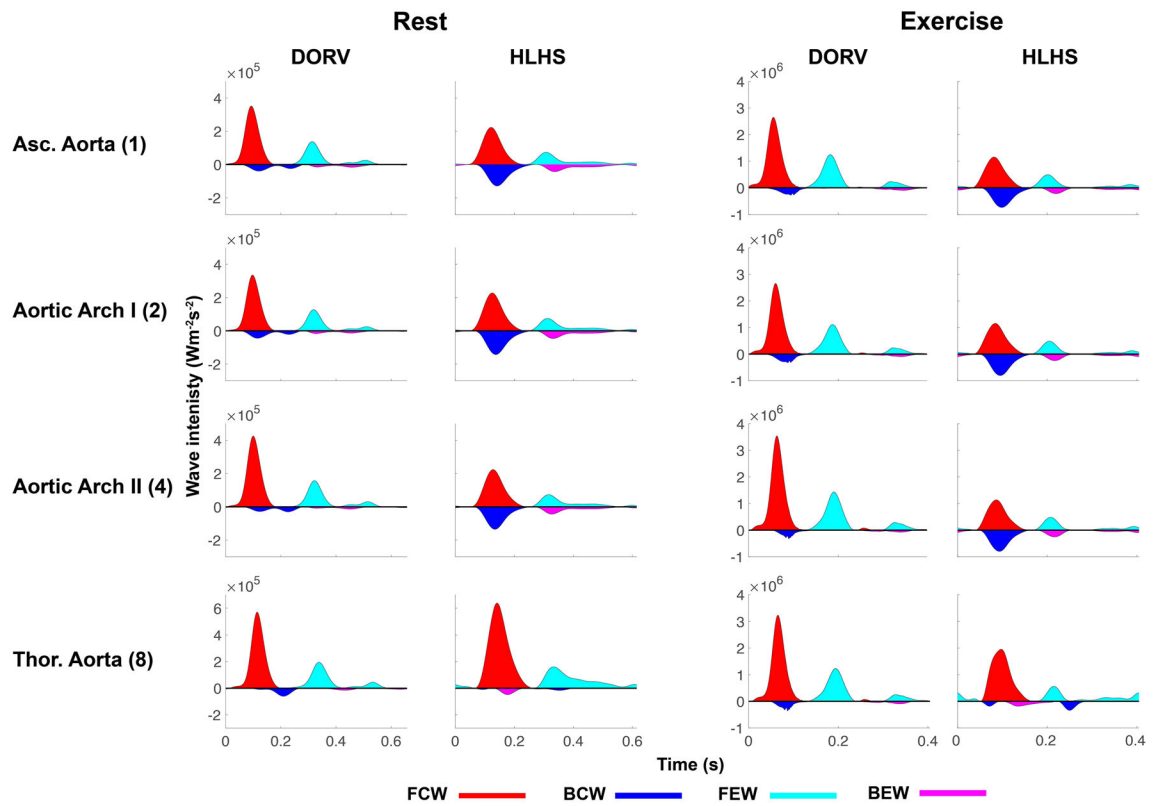
Fig. 10.
Wave intensity analysis at the midpoint of each aortic vessel segment at supine rest and light upright exercise. Results for both patients show a predominant forward traveling wave in each vessel. The HLHS patient has larger backward traveling waves, while the DORV patient has relatively minor backward traveling waves
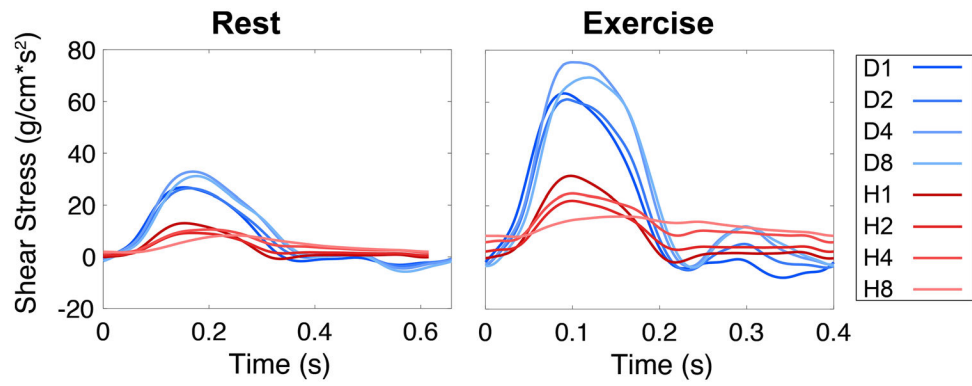
Fig. 11.

WSS results within the aortic vessels. The DORV patient is shown in blue and the HLHS patient in red. During supine rest, WSS values for the DORV patient have a maximum of $\sim30-35$ g/cm/s^2 while values for the HLHS patient have a maximum of $\sim10-15$ g/cm/s^2. During light upright exercise, WSS values for the DORV patient have a maximum of $\sim75-80$ g/cm/s^2, while WSS values for the HLHS patient have a maximum of $\sim30-40$ g/cm/s^2

Table 1

Age, height, weight, blood pressures, and cardiac cycle duration for the DORV and HLHS patients

	DORV	HLHS
Age (years)	12	11
Height (cm)	154.3	151.4
Weight (kg)	59.6	62.0
Systolic pressure (mmHg)	110	116
Diastolic pressure (mmHg)	67	65
Cardiac cycle length (s)	0.658	0.615

Cuff pressures were obtained using a sphygmomanometer from the upper arm in the supine position. These pressures approximate the systolic and diastolic pressures of the brachial artery in the supine rest position. The cardiac cycle duration was measured at the time of the 4D-MRI acquisition in the supine rest position

Table 2

Average flow data from the 4D-MRI images before and after scaling to ensure mass conservation

Vessel	DORV				HLHS			
	Data	Scaled	Abs.	Rel. (%)	Data	Scaled	Abs.	Rel. (%)
Inflow	4.06	4.06	0	0	5.08	5.08	0	0
Asc. Aorta	4.14	4.06	0.08	1.93	4.49	5.08	0.59	13.14
Aortic Arch I	3.69	3.32	0.37	10.03	4.75	4.51	0.24	5.05
Aortic Arch II	4.22	3.13	1.09	25.83	4.16	4.12	0.04	0.96
Thoracic Aorta	2.95	2.62	0.33	11.19	3.67	3.67	0	0
Brachiocephalic	1.95	0.75	1.2	61.54	1.04	0.56	0.48	30.77
L Comm. Carotid	1.19	0.19	1.00	84.03	0.54	0.40	0.14	25.93
L Subclavian	0.82	0.50	0.32	39.02	0.74	0.45	0.29	39.19

Values listed are in L/min. Abs. and Rel. refer to the absolute and relative changes in the flows respectively

Table 3

Vessel names and dimensions used in this study

Number	Name	DORV			HLHS		
		L (cm)	R_{in} (cm)	R_{out} (cm)	L (cm)	R_{in} (cm)	R_{out} (cm)
1	Ascending aorta	4.07	1.20	1.10	3.87	1.96	1.88
2	Aortic arch I	1.95	1.10	0.95	1.93	1.88	1.55
3	Brachiocephallic	1.23	0.25	0.25	1.60	0.35	0.35
4	Aortic arch II	1.94	0.95	0.88	3.77	1.55	1.44
5	L common carotid	20.23	0.25	0.25	20.10	0.31	0.31
6,11	Vertebral	14.4	0.20	0.19	14.3	0.20	0.20
7,9	Subclavian	3.67	0.25	0.25	3.27	0.25	0.25
8	Thoracic aorta	15.17	0.88	0.59	15.07	1.44	0.59
10,17	Brachial	20.23	0.35	0.30	20.10	0.20	0.20
12,14	External carotid	17.22	0.25	0.25	17.01	0.25	0.20
13,15	Internal carotid I	17.12	0.25	0.25	17.01	0.20	0.20
16	R common carotid	17.22	0.25	0.25	17.10	0.20	0.20
18	Basilar	2.76	0.15	0.15	2.74	0.15	0.15
19,20	PCA I	0.48	0.10	0.10	0.47	0.10	0.10
21,23	PCA II	8.18	0.10	0.10	8.13	0.10	0.10
22,24	PCoA	1.43	0.07	0.07	1.42	0.07	0.07
25,26	Internal carotid II	0.48	0.19	0.19	0.47	0.19	0.19
27,29	MCA	11.32	0.14	0.14	11.24	0.14	0.14
28,30	ACA I	1.14	0.11	0.11	1.13	0.11	0.11
31,33	ACA II	9.8	0.11	0.11	9.73	0.11	0.11
32	ACoA	0.29	0.07	0.07	0.28	0.07	0.07
34	Celiac axis	1.95	0.37	0.37	1.93	0.37	0.37
35	Abdominal aorta	5.16	0.59	0.57	5.12	0.59	0.47
36	Superior mesenteric	5.74	0.29	0.29	5.70	0.29	0.29
37	Abdominal aorta	0.97	0.57	0.55	0.97	0.57	0.55
38,40	Renal	3.11	0.25	0.25	3.09	0.25	0.25
39	Abdominal aorta	0.97	0.55	0.53	0.97	0.55	0.53
41	Abdominal aorta	10.31	0.53	0.51	10.24	0.53	0.50
42	Inferior mesenteric	4.86	0.16	0.16	4.83	0.15	0.15
43	Abdominal aorta	0.97	0.51	0.48	0.97	0.50	0.48
44,45	External iliac	14.01	0.27	0.26	13.91	0.27	0.26
46,48	Internal iliac	4.86	0.26	0.26	4.83	0.26	0.26
47,49	Femoral	13.09	0.24	0.21	13.00	0.21	0.21
50,52	Femoral	43.09	0.21	0.21	42.81	0.21	0.21
51,53	Deep femoral	12.26	0.15	0.12	12.17	0.14	0.12
54	Splenic	5.99	0.21	0.19	5.95	0.21	0.19
55	Celiac axis	1.90	0.25	0.25	1.89	0.25	0.25
56	Left Gastric	6.75	0.15	0.14	6.71	0.15	0.14

Number	Name	DORV			HLHS		
		L (cm)	R_{in} (cm)	R_{out} (cm)	L (cm)	R_{in} (cm)	R_{out} (cm)
57	Hepatic	6.28	0.26	0.21	6.24	0.26	0.21

Vessel numbers correspond to numbers given in Fig. 3

Table 4

Stiffness and structured tree parameters for the arterial network

Nominal parameter values	
k_1	2.0×10^6 g/s^2 cm
k_2	-35 cm^{-1}
k_3	3.80×10^5 g/s^2 cm
r_{min}	0.01 cm
α	0.90
β	0.60
lrr	50

	Tuned r_{min} (cm)	
Vessel number	**DORV**	**HLHS**
10,17	0.03	0.03
12,14	0.001	0.001
21,23	0.001	0.001
27,29	0.001	0.001
31,33	0.001	0.001
46,48	0.01	0.10
47,49	0.01	0.10
50,52	0.01	0.10
51,53	0.01	0.10

	Tuned k_3 (g/cm/s^2)	
Vessel number	**DORV**	**HLHS**
1	3.8×10^5	5.7×10^5
2	3.8×10^5	5.7×10^5
4	3.8×10^5	5.7×10^5
5,16	3.8×10^5	4.56×10^5
6,11	7.6×10^5	1.9×10^6
7,9	3.8×10^5	5.7×10^5
8	3.8×10^5	5.7×10^5

3.8×10^5	7.6×10^5	10,17
2.66×10^6	2.66×10^6	12,14
2.66×10^6	2.66×10^6	13,15
2.66×10^6	1.9×10^6	21,23
3.04×10^5	3.8×10^5	35,37,39,41,43
3.04×10^5	3.8×10^5	44–52

Parameter values were nominally set to be consistent between DORV and HLHS patients. Specific values were found by manual tuning for particular vessels to fit flow predictions to patient data

Table 5

Percentage of stroke volume flowing to the brain, liver and gut, lower body, and other regions

Region	Rest		Exercise	
	DORV (%)	HLHS (%)	DORV (%)	HLHS(%)
Cerebral	8.6	7.3	4.8	5.2
Liver and gut	24.3	15.7	20.2	9.4
Lower body	25.7	48.0	40.0	60.8
Other	41.4	29.0	35.0	24.6

These values are shown as percentages of the stroke volume

Table 6

Wave reflection coefficients (I_R) computed for the aortic vessels

Region	Rest		Exercise	
	DORV	**HLHS**	**DORV**	**HLHS**
Ascending aorta	0.567	0.834	0.359	0.816
Aortic arch I	0.583	0.830	0.389	0.835
Aortic arch II	0.483	0.788	0.310	0.819
Thoracic aorta	0.389	0.170	0.377	0.347